Supporting information for: Morphology-Dependent Energy Transfer Dynamics in Fluorene-Based Amphiphile Nanoparticles

Amy L. Stevens,[†] Adrien Kaeser,[‡] Albertus P. H. J. Schenning,[‡] and Laura M. Herz[*,†]

Clarendon Laboratory, Parks Road, Oxford OX1 3PU, United Kingdom, and Laboratory for Functional Organic Materials and Devices, Eindhoven University of Technology, P.O. Box 513, 5600 MB Eindhoven, The Netherlands

E-mail: l.herz1@physics.ox.ac.uk

Synthesis and Characterisation of AMP1-N and AMP1-B

AMP1-N. Based on a literature procedure,[1,2] **1** (150 mg, 0.14 mmol, 1eq.) reacted with **3** (198 mg, 0.28 mg, 2 eq.) and **4** (217 mg, 0.28 mmol, 2 eq.), yielding **Amp1-N** (112 mg, 0.05 mmol, 32 %) as a colorless solid, purified by column chromatography (SNAP 25, MeOH 0 % to 5 % in CH_2Cl_2) and preparative recycling GPC. ^{1}H NMR (400 MHz, THF-d_8) δ 8.02-8.04 (m, 2H), 7.75-7.84 (m, 6H), 7.51-7.56 (m, 7H), 7.41-7.43 (m, 3H), 7.11 (s, 2H), 4.28 (br, 6H), 4.02-4.08 (m, 6H), 3.54-3.89 (m, 36H), 3.35-3.40 (m, 8H), 1.96-2.10 (m, 8H), 1.67-1.87 (m, 14H), 1.03-1.51 (m, 84H), 0.86-0.90 (m, 14H), 0.58-0.82 (m, 44H); ^{13}C NMR (100 MHz, $CDCl_3$) δ 165.52, 165.19, 162.45, 162.27, 153.13, 153.11, 152.68, 152.48, 152.43, 152.09, 151.90, 150.46, 150.44, 144.13,

[*]To whom correspondence should be addressed
[†]Clarendon Laboratory, Oxford, UK
[‡]Laboratory for Functional Organic Materials and Devices, Eindhoven University of Technology

143.97, 141.71, 141.37, 140.21, 140.08, 139.94, 139.07, 138.94, 137.84, 137.42, 137.26, 137.02, 132.13, 132.12, 130.22, 129.99, 128.68, 128.64, 126.45, 126.34, 125.63, 124.80, 123.35, 122.93, 120.01, 119.91, 119.16, 119.10, 118.86, 114.91, 114.72, 110.06, 108.97, 107.73, 105.85, 73.46, 72.31, 71.84, 71.82, 71.80, 70.72, 70.48, 70.44, 70.42, 70.40, 70.38, 69.71, 69.39, 69.26, 69.09, 68.97, 58.90, 58.85, 55.11, 55.08, 39.12, 39.11, 37.66, 36.91, 36.86, 36.69, 36.64, 33.05, 32.99, 32.90, 31.86, 31.84, 30.26, 29.65, 29.63, 29.62, 29.57, 29.54, 29.52, 29.34, 29.32, 29.31, 29.29, 27.79, 26.03, 24.68, 24.66, 24.63, 22.60, 22.59, 22.49, 22.46, 19.67, 19.66, 19.35, 19.32, 14.04; MALDI TOF MS: calc. [M+] 2426.79, found 2426.59.

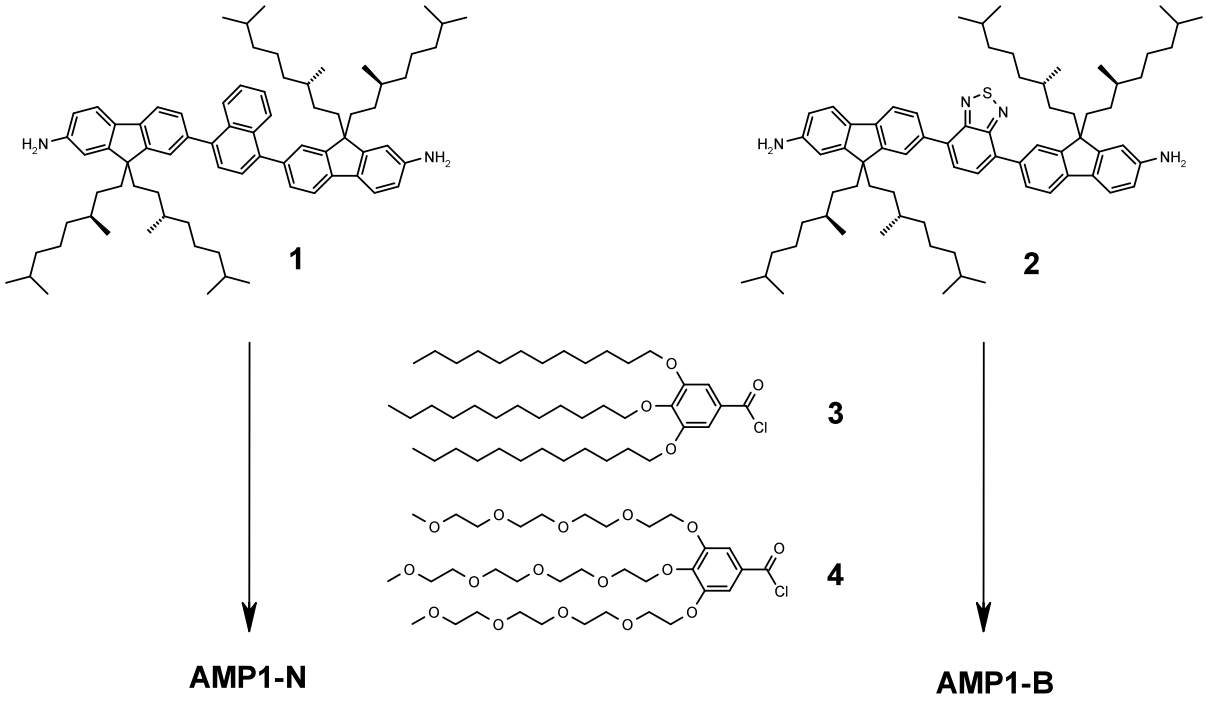

Figure 1: Reaction scheme for synthesis of **AMP1-N** and **AMP1-B**.

AMP1-B. AMP1-N. Based on a literature procedure,[1,2] **2** (200 mg, 0.2 mmol, 1 eq.) reacted with **3** (304 mg, 0.4 mg, 2 eq.) and **4** (334 mg, 0.4 mmol, 2 eq.), yielding **Amp1-B** (112 mg, 0.05 mmol, 32 %) as a yellow solid, purified by column chromatography (SNAP 25, MeOH 0 % to 5 % in CH_2Cl_2) and preparative recycling GPC. ^{1}H NMR (400 MHz, $CDCl_3$) δ 8.44 (br, 1H), 8.03 (d, ^{3}J = 7.89 Hz, 2H), 7.93 (s, 2H), 7.80-7.86 (m, 7H), 7.74 (dd, ^{3}J = 8.1 Hz, ^{4}J = 2.0 Hz, 2H), 7.63 (d, ^{3}J = 7.6 Hz, 1H), 7.56 (dd, ^{3}J = 8.2 Hz, ^{4}J = 1.6 Hz, 1H), 7.29 (s, 2H), 7.11 (s, 2H), 7.23-7.27

(m, 6H), 4.02-4.08 (m, 6H), 3.87 (t, ^{3}J = 4.5 Hz, 4H), 3.81 (t, ^{3}J = 4.8 Hz, 2H), 3.61-3.74 (m, 30H), 3.51-3.56 (m, 6H), 3.38 (s, 3H), 3.33 (s, 6H), 1.97-2.16 (m, 8H), 1.73-1.87 (m, 9H), 1.45-1.53 (m, 6H), 1.27-1.41 (m, 52H), 0.97-1.21 (m, 24H), 0.86-0.92 (m, 12H), 0.59-0.79 (m, 42H); ^{13}C NMR (100 MHz, $CDCl_3$) δ 165.43, 165.17, 154.35, 153.26, 152.57, 152.54, 152.34, 150.94, 141.94, 141.57, 141.12, 140.97, 137.90, 137.51, 137.20, 136.97, 135.84, 135.72, 133.60, 133.52, 130.27, 130.06, 128.19, 128.17, 127.75, 127.73, 123.82, 120.31, 120.23, 119.33, 119.28, 119.06, 118.80, 114.87, 114.67, 107.88, 105.90, 73.56, 72.40, 71.93, 71.89, 70.67, 70.66, 70.60, 70.57, 70.54, 70.49, 70.48, 69.81, 69.53, 69.28, 59.01, 58.96, 55.28, 55.23, 39.22, 39.20, 39.20, 36.85, 36.79, 36.59, 36.54, 33.05, 32.99, 32.96, 32.94, 31.93, 31.91, 30.77, 30.70, 30.68, 29.74, 29.74, 29.72, 29.69, 29.65, 29.64, 29.58, 29.40, 29.38, 29.35, 27.89, 27.88, 26.08, 24.78, 24.70, 24.61, 24.59, 22.69, 22.68, 22.65, 22.63, 22.54, 22.51, 19.69, 19.67, 19.43, 19.39, 14.10; MALDI TOF MS: calc. [M+] 2434.73, found 2434.57, 2457.55 [M-Na+], 2472.54 [M-K+].

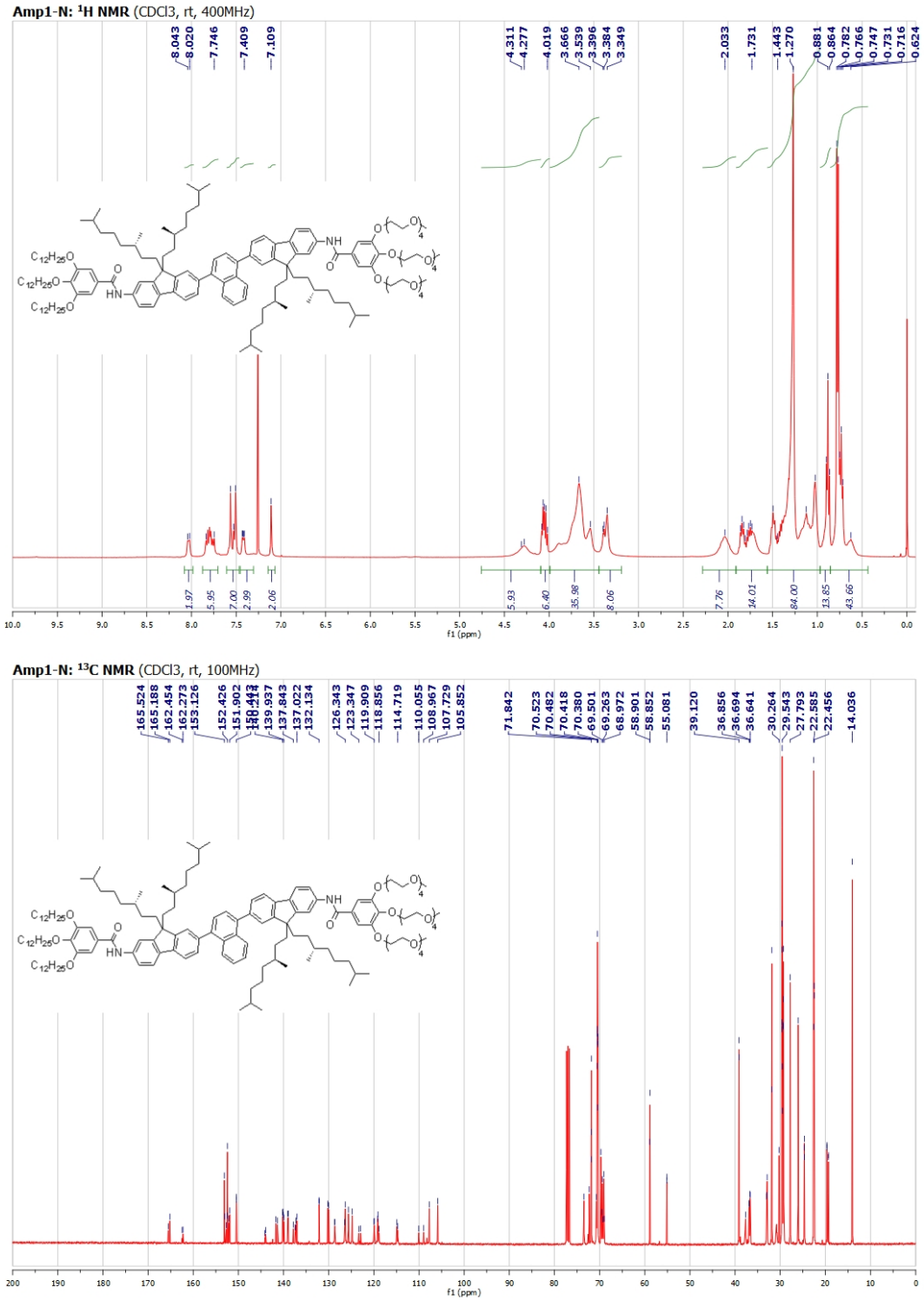

Figure 2: NMR spectra for **AMP1-N**.

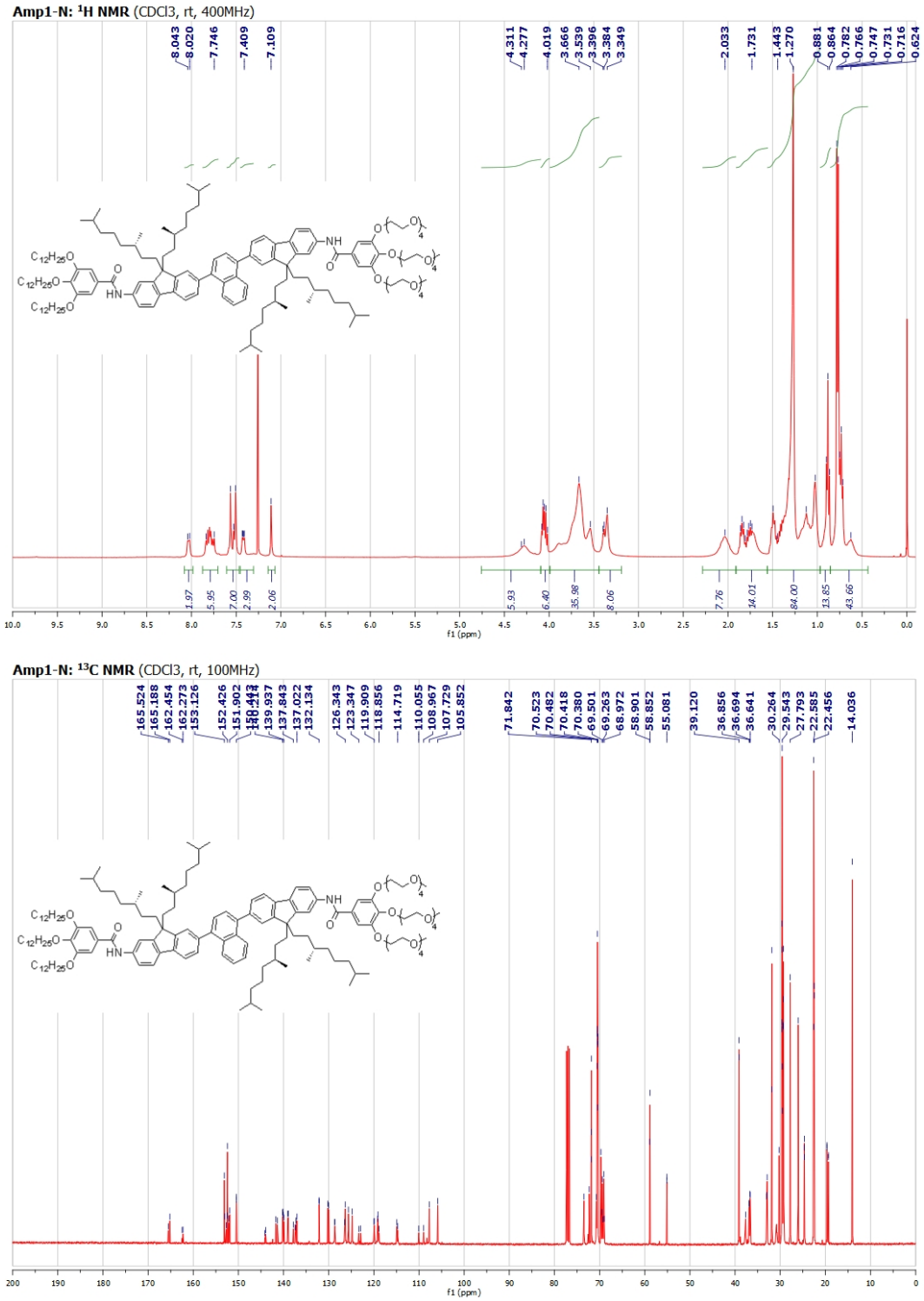

Figure 3: NMR spectra for **AMP1-B**.

Spectral changes upon nanoparticle formation

Figure 4 shows the absorption spectra for AMP1-N and AMP1-B in both the molecularly dissolved phase (in THF) and as nanoparticles following injection into water. Spectral broadening and the appearance of a red shoulder are observed upon nanoparticle formation, which can be attributed to the formation of H-aggregates.

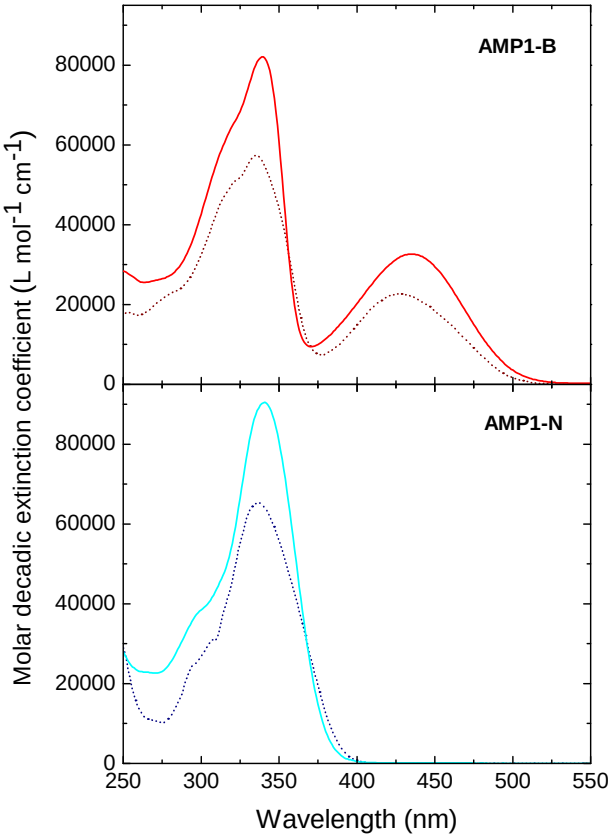

Figure 4: Molar decadic extinction spectra for AMP1-B molecularly dissolved in THF (red solid line) or when injected into water for nanoparticle formation (dark red dotted line); and for AMP1-N molecularly dissolved in THF (cyan line) or when injected into water for nanoparticle formation (dark blue dotted line).

Characterization of AMP1-B Nanoparticles

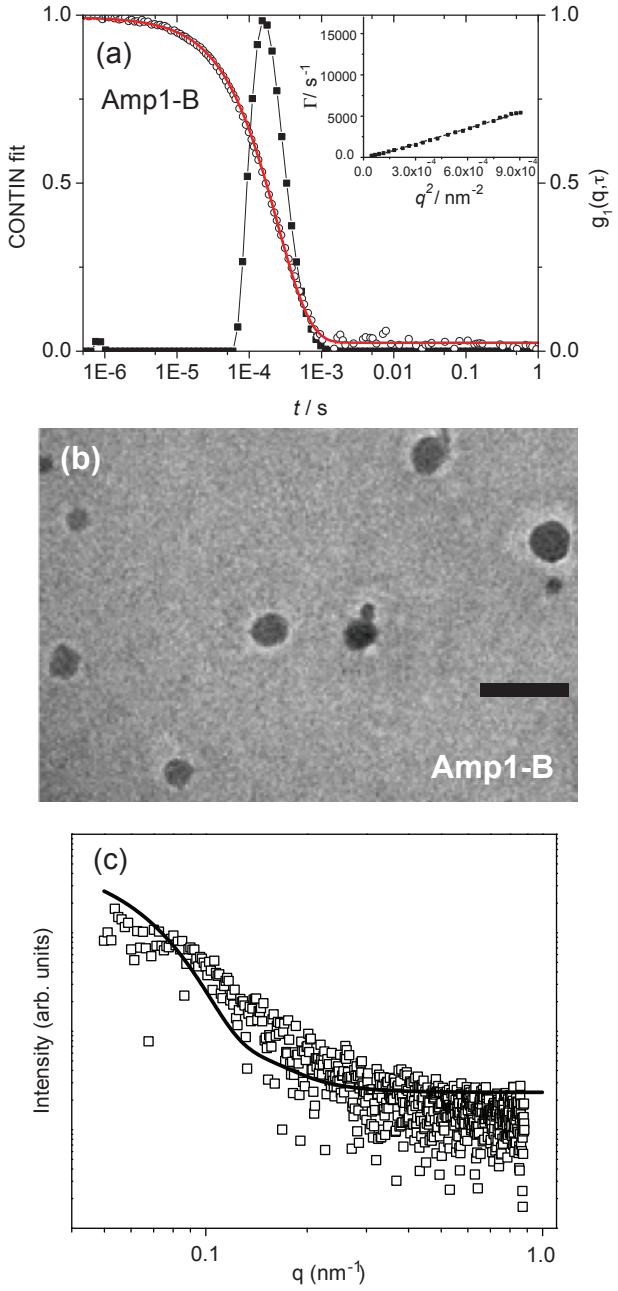

Figure 5: Characterization data for AMP1-B nanoparticles: (a) Multi-angle dynamic light scattering (DLS) data. A hydrodynamic radius of 39.9±0.4 nm was extracted from CONTIN fits of the 150° correlation function and single exponential fits of angular data (see inset). (b) Transmission electron microscopy (TEM) image of AMP1-B nanoparticles. The scale bar represents 200 nm. It should be noted that in dry TEM the deposited particles flatten out on the surface. (c) Small-angle X-ray scattering (SAXS) profile of AMP1-B nanoparticles in solution. The best fit (solid line) to the data is achieved assuming the presence of sherical particles with radius of 40 nm.

Circular Dichroism Spectra

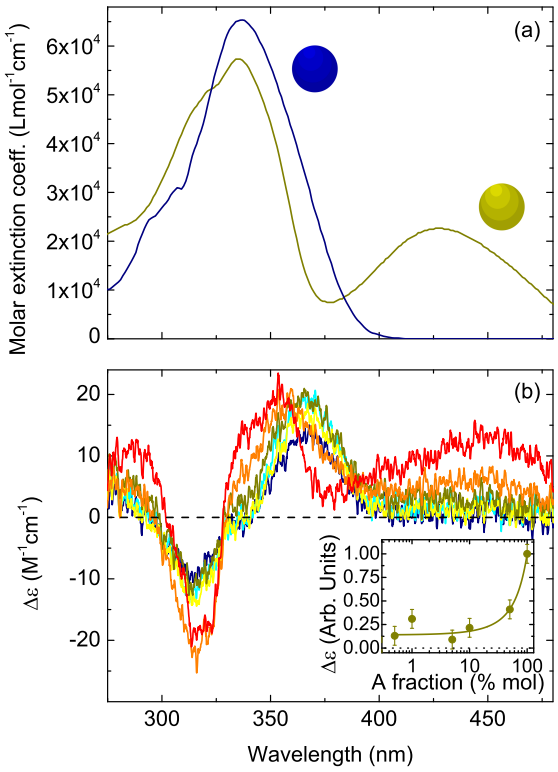

Figure 6: (a) UV-Vis absorption spectra of one-component nanoparticles containing either solely AMP1-N donor molecules (navy line) or solely AMP1-B acceptor molecules (yellow line). The cartoons depict the spherical nature of the nanoparticles. (b) Molar circular dichroism ($\Delta\varepsilon$) spectra of two-component nanoparticle samples. The navy, cyan, yellow, dark yellow, orange, and red lines correspond to AMP1-B acceptor fractions of 0, 0.5, 5, 10, 50, and 100%, respectively. The inset shows normalized values of $\Delta\varepsilon$ integrated from 430 nm to 500 nm, i.e. to the long-wavelength side of the acceptor absorption peak.

Figure 6a shows the absorption spectra for single component nanoparticles containing either just AMP1-N or just AMP1-B. Figure 6b contrasts these absorption spectra with the molar circular dichroism (CD) spectra for two-component blend samples of AMP1-N and AMP1-B for different concentrations of incorporated AMP1-B acceptor ranging from 0% to 100%. Clear but relatively weak bisignate Cotton effects are observed, centred around the various absorption peaks, suggesting that the side chains introduce some helicity into the formation of acceptor aggregate

domains.[3,4] For the spectral region of 250–400 nm, analysis of the CD spectra is complicated by the fact that both AMP1-N and AMP1-B have overlapping absorption peaks. However, the AMP1-B acceptor shows a clear further peak at ∼430 nm whose long-wavelength end does not overlap with any of the AMP1-N donor absorption. Hence, in order to obtain a measure of the presence of acceptor domains with a certain degree of helical molecular stacking, we integrated the CD signal for the long-wavelength side of the peak (430 to 500 nm) as shown in the inset to Figure 6b. The integrated CD signal amplitude for acceptor domains increases as the fraction of acceptors incorporated into the two-component nanoparticle blends is raised beyond a few percent. These results support the notion that significant acceptor phase segregation occurs with increasing acceptor concentration. However, it should be noted that even at lower acceptor concentrations, such segregation may be present in less ordered form that may not necessarily give rise to a CD signal.

Donor emission quenching in presence of acceptor

As an initial analytical approach to investigating the energy transfer processes involved in the two-component nanoparticles, dynamic and static quenching were considered. Figure 7 presents the ratio I_0/I plotted against $[Q]$, where Q is the quencher (*i.e.* AMP1-B acceptor) concentration, while I_0 and I are the fluorescence intensity of the AMP1-N donor molecules (at emission wavelength 421 nm) in the absence and in the presence of quencher, respectively. At low quencher concentration (0.5 to 10% of Amp1-B, corresponding to Q=1.5 – 30×10^{-8}M) the curve diverges with a upward curvature from a linear trend, thus preventing a correlation to be made between the energy transfer process observed and a dynamic Stern-Volmer quenching meachnism. Likewise, the quenching processes cannot be explained in terms of static quenching, as the variation of $\ln(I_0/I)$ against $[Q]$ exhibits a downward curvature, as opposed to the linear behavior expected (see Figure 7).

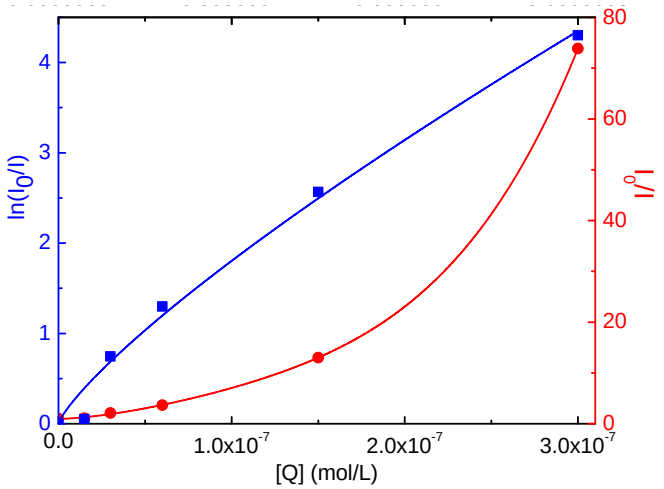

Figure 7: Plot of relative donor (AMP1-N) emission quenching in the presence of acceptor (AMP1-B) at concentration $[Q]$. The red circles give the ratio of the donor emission intensities at 421 nm in the absence of acceptor (I_0) to that in the presence of acceptor (I). The blue squares show the concentration dependence of the natural logarithm of this ratio. Solid lines are guides to the eye. The total concentration of molecules was kept constant for the experiment.

Time-resolved acceptor photoluminescence

Figure 8 shows the decay of the photoluminescence emitted from one-component nanoparticle blends and two-component blend nanoparticles. Here, the detection wavelength was set to the peak of the AMP1-B acceptor emission spectrum (575 nm), however, even at 0% acceptor fraction a sizeable signal is evident. This decay must originate from the AMP1-N donor emission, as no other species is present, and is caused by the sizeable overlap between the long low-energy tail of the donor emission with most of the acceptor emission spectrum (see main article). Since the acceptor-only (100%) nanoparticle emission lifetime is substantially longer than that of the donor-only (0%) nanoparticles, an increasing contribution to the emission from acceptors will increase the lifetime of the emission detected at 575 nm even in the absence of energy transfer. For one-component nanoparticle blends, donor emission decays and time-integrated emission spectra discussed in the main article strongly suggest the absence of energy transfer between AMP1-N and AMP1-B nanoparticles. The changes in one-component nanoparticle emission dynamics measured at the acceptor peak (Figure 8a) are therefore most likely solely caused by changes in the overall contribution to the total emission from the two species. For these reasons, the emission dynamics

at the acceptor peak measured for the two-component nanoparticles (Figure 8b) also have to be taken with great care. Here a much faster switch-over from fast to slow decay dynamics with increasing acceptor fraction is observed. Fast excitation transfer from donor to acceptor molecules will here lead to longer acceptor emission life times, however, such transfer will also depopulate donor molecules that contribute shorter-lived emission at the same wavelength and give a similar effect. The data are therefore qualitatively in agreement with efficient energy transfer occurring in the two-component nanoparticles. However, since the two contributing effects cannot be easily disentangled, the donor emission was used in our study in order to analyse the energy transfer dynamics for these materials (see main article).

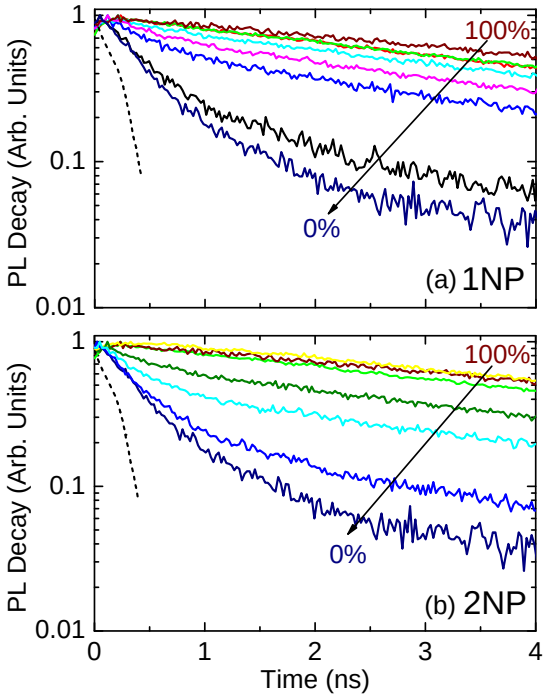

Figure 8: Normalized time-resolved photoluminescence decays of (a) single-component nanoparticle (1NP) blends and (b) two-component nanoparticles (2NP) measured at the AMP1-B acceptor emission peak wavelength (575 nm). The acceptor proportions in the 1NP blend samples are 100, 90, 75, 50, 25, 10, 1, and 0% and in the 2NP samples are 100, 5, 0.5, 0.12, 0.03, 0.01, and 0%. The dashed curves represent the instrument response function.

Dimensionality of energy transfer in the nanoparticles

Theoretical models for the excitation migration in conjugated molecular materials often yield solutions following stretched-exponential behaviour,[5–7] i.e. the surviving exciton population can be described by

$$I(t) = I_0 \exp\left(-\left[\frac{t}{t_0}\right]^{\alpha}\right) \tag{1}$$

corresponding to an effective transfer rate for the donor-acceptor ensemble of:

$$k_{ens}(t) = \alpha t_0^{-\alpha} t^{\alpha-1}. \tag{2}$$

Förster's original theory of resonance excitation energy transfers predicted such stretched exponential dynamics with $\alpha = 0.5$ for donors and acceptors randomly distributed in three dimensions.[6] This is because the Förster energy transfer rate for an *individual* donor-acceptor pair separated by a distance R is given by

$$k_{DA}(t) = \frac{1}{\tau_D}\left(\frac{R_0}{R}\right)^6 \tag{3}$$

where R_0 is the Förster radius[8] and τ_D the natural lifetime of the donor in absence of acceptors. Therefore, excitations located close to an acceptor will undertake transfer with a faster rate than those located further away, such that the *ensemble-averaged* rate appears to slow with time. Photoexcitation will initially create a population of excitations that are randomly distributed in the host, but as time progresses this distribution becomes increasingly non-random as only those excitations survive that are located far from guests.[9] The ensemble rate of energy transfer therefore has a direct link with the statistical distribution of donor-acceptor distances present in that ensemble. For randomly distributed acceptors within a donor matrix, the dimensionality of the system has been shown to have an impact on the statistical distribution of R,[10,11] with the resulting α given by $\alpha = \frac{\Delta}{6}$ where Δ is the number of dimensions in the system, i.e. $\alpha = \frac{1}{2}, \frac{1}{3}$ or $\frac{1}{6}$ for a three-, two- or one-dimensional system, respectively.[7] Representing the energy transfer dynamics (displayed in Figure 6 of the main article) in Kohlrausch-Williams-Watts (KWW) representation[12,13] (for which

the logarithm of $\ln(I_0/I)$ is plotted against the logarithm of time after excitation) allows direct examining of the slope α prevalent in the energy transfer processes. As described in the main article, the experimental energy transfer dynamics were obtained by dividing the AMP1-N donor emission from the two-component nanoparticles by the emission from donor-only nanoparticles to reflect the donor excitation decay solely attributable to energy transfer. These transient are plotted in Figure 9 together with solid lines given by Eqn. 1 for energy transfer in three-, two- and one-dimensional systems of randomly distributed donors and acceptors. It is evident that the data follow a trend most closely to that for energy transfer in a three-dimensional random arrangement of acceptors inside the donor matrix, in particular for the lower acceptor concentration range. This result is to be expected given that the nanoparticles have significantly larger diameters (80 nm) than the Förster radius deduced from spectral overlap calculations (R_0=2.9 nm – see main article). For higher incorporated acceptor fractions ($<$1%) deviations in particular at longer times after excitation are found, in agreement with substantial clustering of acceptor molecules into domains, as indicated by changes in acceptor emission and circular dichroism absorption spectra. As long as the formed domains are small compared to average donor-acceptor energy transfer distances, a material may still be viewed as being composed of random acceptor sites placed in a donor matrix (albeit at a reduced effective acceptor concentration). However, when acceptor domains become more comparable in size to donor domains, such assumptions of random distributions must break down, as apparent in Figure 9. Additional deviations from stretched exponential behaviour with α=0.5 occur at very early times, for which the effective value of α appears to be larger than 0.5. Such behaviour has previously been observed in organic conjugated solids comprised of acceptors dispersed in a donor matrix, for which it was attributed to strong excitation diffusion in the donor matrix which aids the overall energy transfer dynamics while excitations are initially highly mobile.[13] The overall shape of the transfer dynamics at low incorporated acceptor fractions are therefore in agreement with fast exciton diffusion inside a donor matrix in which acceptor molecules are randomly distributed within three dimensions.

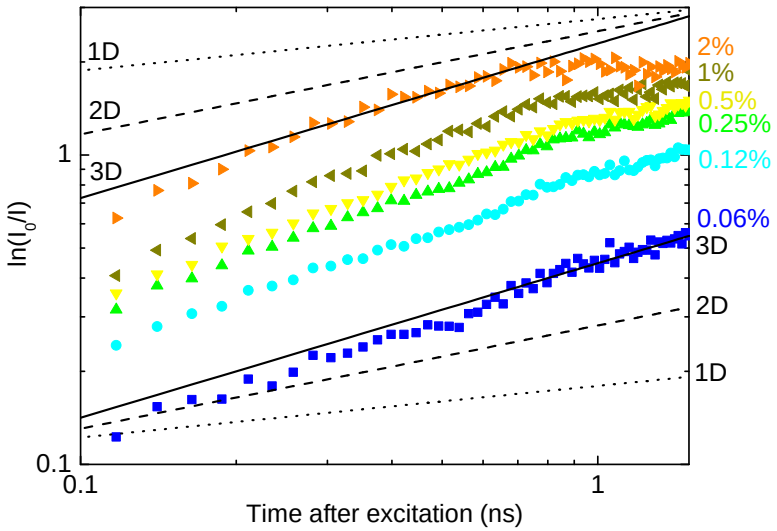

Figure 9: A Kohlrausch-Williams-Watts representation of the excitation transfer decays of two-component nanoparticles, shown in Figure 6a (main paper), for varying mole fractions of incorporated acceptor. The solid, dashed, and dotted lines represent a system dimensionality of 3, 2, and 1, respectively.

References

1. Abbel, R.; van der Weegen, R.; Pisula, W.; Surin, M.; Leclère, P.; Lazzaroni, R.; Meijer, E. W.; Schenning, A. P. H. J. Multicolour self-assembled fluorene co-oligomers: from molecules to the solid state via white-light-emitting organogels. *Chem.-Eur. J.* **2009**, *15*, 9737–9746.

2. Abbel, R.; van der Weegen, R.; Meijer, E. W.; Schenning, A. P. H. J. Multicolour self-assembled particles of fluorene-based bolaamphiphiles. *Chem. Commun.* **2009**, *0*, 1697–1699.

3. Hoeben, F. J. M.; Shklyarevskiy, I. O.; Pouderoijen, M. J.; Engelkamp, H.; Schenning, A. P. H. J.; Christianen, P. C. M.; Maan, J. C.; Meijer, E. W. Direct visualization of efficient energy transfer in single oligo(*p*-phenylene vinylene) vesicles. *Angew. Chem.-Int. Edit.* **2006**, *45*, 1232–1236.

4. Behanna, H. A.; Rajangam, K.; Stupp, S. I. Modulation of fluorescence through coassembly of molecules in organic nanostructures. *J. Am. Chem. Soc.* **2007**, *129*, 321–327.

5. Movaghar, B.; Grunewald, M.; Ries, B.; Bässler, H.; Wurtz, D. Diffusion and relaxation of energy in disordered organic and inorganic materials. *Phys. Rev. B* **1986**, *33*, 5545–5554.

6. Förster, T. Experimentelle und theoretische Untersuchung des zwischenmolekularen Übergangs von Elektronenanregungsenergie. *Z. Naturforsch.* **1949**, *4a*, 321.

7. Parkinson, P.; Aharon, E.; Chang, M. H.; Dosche, C.; Frey, G. L.; Köhler, A.; Herz, L. M. Dimensionality-dependent energy transfer in polymer-intercalated SnS_2 nanocomposites. *Phys. Rev. B* **2007**, *75*, 165206.

8. Förster, T. H. 10th Spiers Memorial Lecture. Transfer mechanisms of electronic excitation. *Discuss. Faraday Soc.* **1959**, *27*, 7–17.

9. Powell, R. C.; Soos, Z. G. Singlet exciton energy transfer in organic solids. *J. Lumines.* **1975**, *11*, 1–45.

10. Baumann, J.; Fayer, M. D. Excitation transfer in disordered two-dimensional and anisotropic three-dimensional systems: effects of spatial geometry on time-resolved observables. *J. Chem. Phys.* **1986**, *85*, 4087–4107.

11. Blumen, A.; Manz, J. On the concentration and time dependence of the energy transfer to randomly distributed acceptors. *J. Chem. Phys.* **1979**, *71*, 4694–4702.

12. Mollay, B.; Lemmer, U.; Kersting, R.; Mahrt, R. F.; Kurz, H.; Kauffman, H. F.; Bässler, H. Dynamics of singlet excitations in conjugated polymers - poly(phenylenevinylene) and poly(phenylphenylenevinylene). *Phys. Rev. B* **1994**, *50*, 10769.

13. Herz, L. M.; Silva, C.; Grimsdale, A. C.; Müllen, K.; Phillips, R. T. Time-dependent energy transfer rates in a conjugated polymer guest-host system. *Phys. Rev. B* **2004**, *70*, 165207.